ELSEVIER

Alzheimer's & Dementia ■ (2019) 1-11

Alzheimer's & Dementia

Featured Article

Amyloid pathology–produced unexpected modifications of calcium homeostasis in hippocampal subicular dendrites

Sergio L. Angulo[a], Thomas Henzi[b], Samuel A. Neymotin[c], Manuel D. Suarez[a], William W. Lytton[a,d], Beat Schwaller[b], Herman Moreno[a,d,*]

[a]*Departments of Neurology and Physiology/Pharmacology, The Robert F. Furchgott Center for Neural and Behavioral Science, SUNY Downstate Medical Center, Brooklyn, NY, USA*

[b]*Anatomy, Department of Medicine, University of Fribourg, Fribourg, Switzerland*

[c]*Nathan Kline Institute for Psychiatric Research, Orangeburg, NY, USA*

[d]*Kings County Hospital, Brooklyn, NY, USA*

Abstract

Introduction: Alzheimer's disease (AD) is linked to neuronal calcium dyshomeostasis, which is associated with network hyperexcitability. Decreased expression of the calcium-binding protein calbindin-D_{28K} (CB) might be a susceptibility factor for AD. The subiculum is affected early in AD, for unknown reasons.

Methods: In AD, CB knock-out and control mice fluorescence Ca^{2+} imaging combined with patch clamp were used to characterize Ca^{2+} dynamics, resting Ca^{2+}, and Ca^{2+}-buffering capacity in subicular neurons. CB expression levels in wild-type and AD mice were also analyzed.

Results: The subiculum and dentate gyrus of wild-type mice showed age-related decline in CB expression not observed in AD mice. Resting Ca^{2+} and Ca^{2+}-buffering capacity was increased in aged AD mice subicular dendrites. Modeling suggests that AD calcium changes can be explained by alterations of Ca^{2+} extrusion pumps rather than by buffers.

Discussion: Overall, abnormal Ca^{2+} homeostasis in AD has an age dependency that comprises multiple mechanisms, including compensatory processes.

Keywords: Alzheimer's disease; Calbindin; Calcium homeostasis; Calcium imaging; Patch clamp; Subiculum

1. Introduction

Alzheimer's disease (AD) starts with episodic memory loss and progresses to functional decline in multiple cognitive domains [1]. The link between specific brain region susceptibility and the pathophysiology of AD is not well understood. In early AD, the subiculum is affected by the amyloidogenic pathology [2,3], which includes decreased number of neurons [4], dendritic loss [5], and neuronal hypersynchrony [6]. The subiculum is involved in memory retrieval and spatial memory [7].

Neuronal Ca^{2+} homeostasis is altered in AD, and it is linked to neuronal susceptibility [8]. Increased intracellular Ca^{2+} levels and neuronal activity were found in neurons close to plaques [9]. The characterization of the Ca^{2+} dynamics of subicular neurons of wild-type (WT) or AD mice remains unknown, and few studies have analyzed how the excessive AD Ca^{2+} levels are handled [9,10]. Most AD mouse models express presenilin mutations that cause *per se* an increase of Ca^{2+} release through IP3 receptors [11], but Ca^{2+} dynamics alterations exclusively produced by amyloidogenic pathology alter the activation of ryanodine receptors [12]. Other possible Ca^{2+} dyshomeostasis mechanisms in AD have been identified [13,14]. The expression of calbindin-D_{28k} (CB) is proposed as a mediator of AD pathophysiology, and it is found decreased

There are no conflicts of interest for any of the authors.

*Corresponding author. Tel.: 718-270-4660.

E-mail address: herman.moreno@downstate.edu

https://doi.org/10.1016/j.jalz.2019.07.017

1552-5260/

in the dentate gyrus (DG) of AD mice [15]; whereas other studies found CB increased expression [16] and increased CB-positive neurons in patients with AD [17]. Yet, no Ca^{2+} dynamics have been described to prove the consequences of CB changes in AD [15,18]. CB is expressed in the subiculum [19], but its expression changes in AD are unknown. In addition, the ability of the neuron to handle calcium inflows, known as Ca^{2+}-buffering capacity [20,21], could be affected during neurodegeneration, but this remains unexplored in AD.

In this study, we evaluated whether increased susceptibility of the subiculum to the amyloidogenic pathology correlates with alterations in the Ca^{2+} homeostasis, and if there were similarities in Ca^{2+} dynamics of AD neurons with those from a mouse lacking CB (CBKO). Fluorescence Ca^{2+} imaging combined with whole-cell patch-clamp were used to characterize Ca^{2+} dynamics, resting Ca^{2+}, and Ca^{2+}-buffering capacity in subicular neurons of young-adult and old mice. In addition, we evaluated the CB expression levels in WT and AD mice. Here, we report the Ca^{2+} dynamics changes observed in AD mice in comparison with CBKO and WT mice. We also used computer models of Ca^{2+} dynamics to investigate the mechanistic origins of the changes observed experimentally and to predict homeostatic compensatory mechanisms involved in AD.

2. Materials and methods

2.1. Animals

Experiments were approved by the Division of Comparative Medicine (DCM) from SUNY Downstate Medical Center. C57Bl/6J mice, AD mouse model (J20) mice, and calbindin (CB) knockout mice (CBKO) were used for the experiments. C57Bl/6J and J20 mice were purchased from The Jackson Laboratory. CBKO animals were provided by Dr. B. Schwaller. Two age groups were studied in these experiments: 1-2 months-old animals serving as the young-adult group (referred as young); and 14-18 months-older-adult (referred as old) animals, 45% males were used for the experiments.

2.2. Electrophysiology and calcium imaging

Animals were anesthetized via i. p. injection with ketamine/xylazine (100/10 mg/kg). The brain was placed in a cold cutting solution bubbled with O_2/CO_2 95/5%, following methods described in previous studies [6, 7]. Horizontal ventral brain slices and recording conditions have also been reported before [6, 7]. Neurons were located at an approximate position: AP -3.8 mm, medio-lateral 3.0 mm, and dorso-ventral -5.6 mm.

For calcium imaging, Oregon Green 488 BAPTA-1 (OG1) was used as a nonratiometric Ca^{2+} indicator and added to the intracellular solution at different concentrations (see Results). In another series of experiments, we used the low-affinity buffer (Oregon Green 488 BAPTA-5N; 500 μM). Subicular pyramidal neurons were recorded in whole-cell configuration in voltage-clamp or current-clamp mode according to the conditions of each experiment, and junction potential was measured and corrected. Neurons were discarded if the leak current was larger than 100 pA at V_h -70 mV or if the access resistance was larger than 20 MΩ. Signals were low-pass filtered at 5 kHz, and offline analysis was performed using Clampfit.

Ca^{2+} signal acquisition and analysis are fully described in Supplementary Material. Because basal fluorescence (F_0) is a critical parameter in our measurements (See Supplementary Material) as an internal control, F_0 was measured in several slices of each experimental group during the time of the data acquisition (after calcium indicator equilibrium, see below) and presented in Fig. 1B (lower panel). No significant changes in F_0 were observed throughout the experiment.

2.3. Immunohistochemistry

Fixed mouse brains were cut horizontally (40 μm), following methods described in Supplementary Material. Tissue was incubated with an anti-CB-D_{28k} antibody (CB38). For the visualization, we used a fluorescent donkey anti-rabbit secondary antibody. Images of the stained sections were taken with a digital slide scanner. Regions of interest were drawn in the DG and subiculum, and densitometry analyses were performed (intensity was normalized by area).

2.4. Computer modeling

We modeled a simplified multicompartment hippocampal pyramidal neuron based on previous models of pyramidal neurons [22,23]. All simulations were run in the NEURON simulation environment using a 0.025 fixed time-step [24] with both electrical modeling and RxD modeling (detailed in Supplementary Material) [25]. The full model of the hippocampal pyramidal neuron is available on ModelDB [26] (http://senselab.med.yale.edu/modeldb).

2.5. Statistical methods

All results were expressed as mean ± standard error of the means, and statistical differences were assumed to exist, if the P value was less than 0.05. Statistical variations in $\Delta F/F_0$ in the text refer to cell-to-cell variations; values of n refer to the number of cells, not the number of regions of interest. We used linear regression models (LRMs), with genotype or group and age or sex as predictors, where indicated. First-order interactions between genotype and age were investigated, and P values were adjusted using the Tukey-Kramer test. In some instances, as indicated in the text, multiple comparisons of parametric data were analyzed using analysis of variance and post hoc test. All analysis used SPSS package.

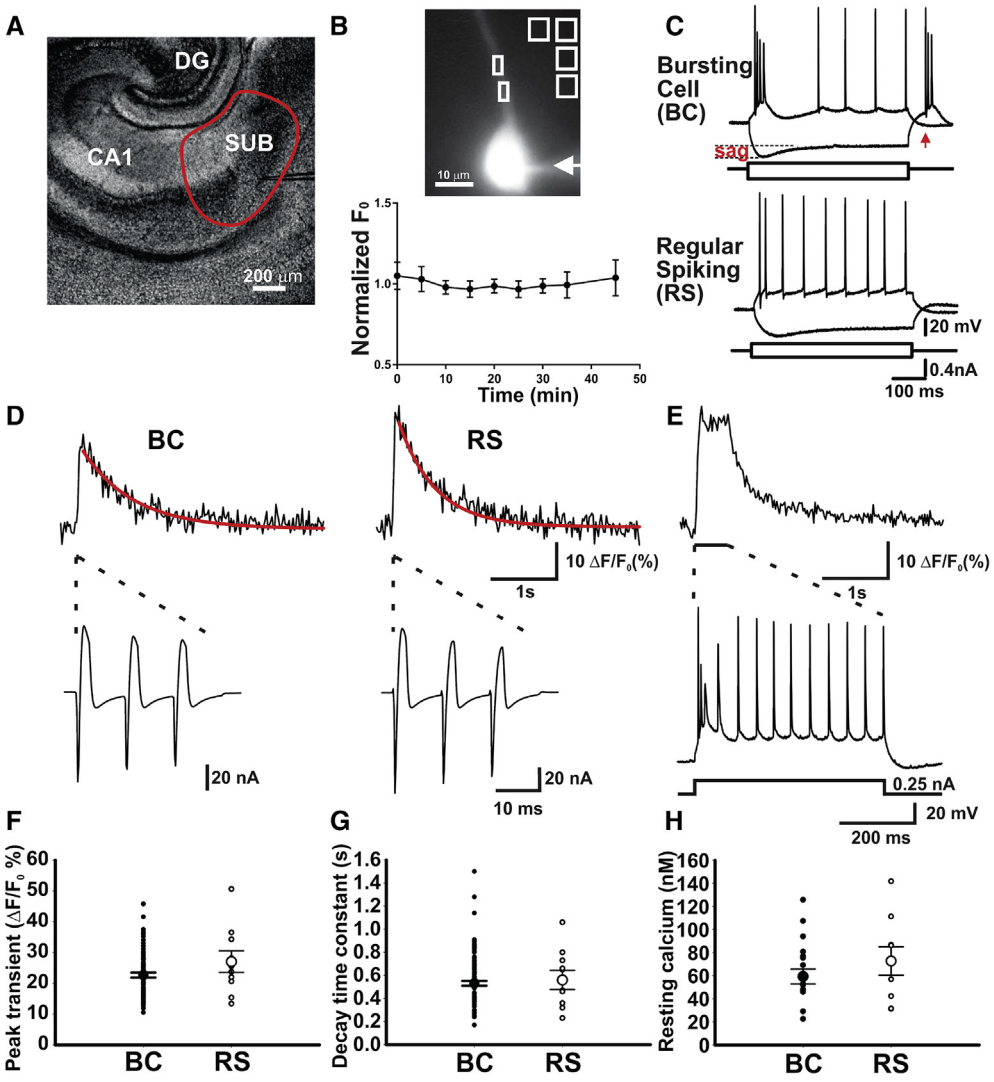

Fig. 1. Ca^{2+} dynamics properties of two electrophysiological subtypes of subicular pyramidal neurons. (A) Microphotograph of slice used, indicating the subiculum in red. (B) **Upper panel:** Ca^{2+} fluorescence image of a subicular pyramidal neuron loaded with Oregon Green BAPTA-1 (OG1; 50 µM in the recording pipette). Arrow indicates the tip of the patch pipette. The squares are regions of interest (ROIs) for the background signal (B), and the rectangles are the ROIs of the apical dendrite signal. **Lower panel:** Normalized basal fluorescence (F_0) against time, and SD values. F_0 was measure once F reached steady state (time 0, typically 16 mins after braking-in) and during 45 mins of 30 randomly selected recordings from all experimental conditions. (C) Representative examples of current-clamp traces in the whole-cell configuration of the patch-clamp technique showing the differences in firing patterns of subicular pyramidal neurons upon current injection as indicated. **Top:** Bursting Cell (BC), the arrow shows rebound action potential; **Bottom:** Regular spiking (RS) cell. (D) **Top:** Ca^{2+} transients evoked by three action potentials (APs) in BC and RS neurons. Mono-exponential fit of the decay in red. **Bottom:** Voltage-clamp traces of evoked rapid depolarization (100 Hz, 3 ms, from -70 mV to +10 mV) in the two neuron types. (E) Ca^{2+} transient plateau induced by a large depolarization in current-clamp (500 ms, 0.25 nA). Note that this parameter is required to calculate the resting Ca^{2+} level (see Methods and Supplementary Material). (F) Scatter plot of peak Ca^{2+} transients, (G) decay time constant, and (H) resting Ca^{2+} concentrations of BC (n = 17) and RS neurons (n = 8); no significant differences were found between the two groups for the peak Ca^{2+} transients, decay time constants, and resting Ca^{2+} concentrations. Abbreviations: DG, dentate gyrus; CA1 subfield; SUB, subiculum.

3. Results

3.1. Electrophysiological properties and Ca^{2+} dynamics of subicular neuron subtypes

Subicular pyramidal neurons (Fig. 1A and B) were recorded for basic electrophysiological and Ca^{2+} imaging experiments. Previous studies have looked at the relative proportions of the various types of subicular neurons identified by their firing properties [7,27]. In the present experiments of young WT mice, the number of bursting cells (BC) recorded (89.3%) was significantly higher than the regular spiking (RS) neurons (10.7%) from a total of 131 neurons analyzed ($X^2_{(1)} = 80.985$, $P < .001$) (Fig. 1C and Supplementary Table 1). Passive membrane properties were compared between BC and RS neurons of young mice. The resting potential and half-width of the first action potential (AP) were similar between BC and RS neurons. But the input resistance and amplitude of the first AP were

significantly different between BC and RS neurons (Supplementary Table 1).

For the next group of experiments, intracellular Ca^{2+} measurements were performed in young WT mice. Similar to studies in axonal varicosities [28], volume-averaged Ca^{2+} (Ca_i) measurements were obtained in apical dendrites using an intracellular solution containing the Ca^{2+} indicator OG1, 50 μM; Fig. 1B. Ca^{2+} transients were evoked by rapid depolarizations (see Supplementary Methods) in BC and RS neurons (Fig. 1D). A total of 109 neurons were used for this analysis, 89.9% were BC, and 10.1% were RS. LRM analysis including the group*sex interaction (see Methods) showed that BC and RS neurons had similar peak Ca^{2+} transients ($F_{(1,107)} = -1.48$, $P = .123$) (Fig. 1F) and a similar mono-exponential decay time constant ($F_{(1,\ 75)} = 0.31$, $P = .685$) (Fig. 1G). The decay time constant was best fitted by a single exponential in 72.2% of RS neurons and in 53.7% of BC neurons. The biexponential fitting of the decay time constant was similar between the two types of neurons (BC fast component $[\tau_f] = 0.248 \pm 0.017$ s, slow component $[\tau_s] = 1.356 \pm 0.141$ s, $As/(As + Af) = 0.5 \pm 0.23$; RS $\tau_f = 0.179 \pm 0.043$ s, $\tau_s = 0.899 \pm 0.111$; $As/(As + Af) = 0.51 \pm 0.08$; fast component $F_{(1,38)} = 1.21$, $P = .244$; slow component $F_{(1,38)} = 0.988$, $P = .371$; $As/(As + Af)$ $F_{(1,38)} = -0.261$, $P = .844$). Ca^{2+} resting levels (Fig. 1E) were not significantly different between BC and RS neurons ($F_{(1,23)} = -1.076$, $P = .312$) (Fig. 1H). No significant group*sex interaction was observed in any of the analysis. In summary, subicular BC and RS neurons have significant differences in the amplitude of the first AP and input resistance, but similar Ca^{2+} dynamics. From this point on, we studied only the more prevalent BC neurons for a comparison between different genotypes.

3.2. Calbindin immunohistochemistry in the DG and subiculum of WT and J20

J20 mice were compared with WT mice. J20 mice overexpress a disease-causing mutation of the human amyloid precursor protein (hAPP) [29]. Calbindin-D_{28k} (CB) is a Ca^{2+}-binding protein with known Ca^{2+}-buffering properties [30]. CB expression levels in young and old J20 and WT mice were determined by immunohistochemistry (IHC) of brain slices. CB staining in the DG was mostly confined to granule cells (Fig. 2A, left panels) and in the subiculum to a population of neurons in the pyramidal cell layer (Fig. 2A, right panels).

LRM analysis shows that IHC signal intensities representing CB expression levels were lower in the DG of old WT mice compared with young ones ($F_{(1,34)} = 6.61$, $P = .008$), whereas there were no significant differences with age in J20 mice ($F_{(1,35)} = 1.37$, $P = .25$) (Fig. 2B). These results are in agreement with our previous study [31], where we had reported an age-dependent loss of CB expression in the DG of WT mice.

In young mice, there was a group difference in the CB signal in the DG, which is lower in J20 mice

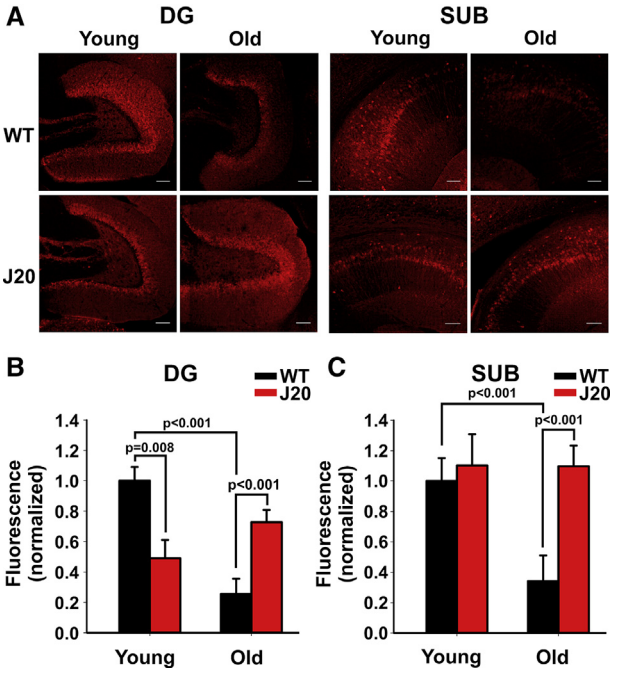

Fig. 2. CB expression levels in the DG and SUB change with age and amyloidogenic pathology. (A) Representative microphotographs of CB immunohistochemistry signal in hippocampal horizontal sections of WT and amyloidogenic model (J20) mice—young-adult (1- to 2-month-olds [WT], n = 20 slices; J20, n = 11 slices) and older-adults (14- to 18-month-olds [WT], n = 16 slices; J20, n = 26 slices). The sections were photographed with a 40X objective, scale bars = 50 μM. CB immunoreactivity intensity (thresholding and densitometry, see Methods and Supplementary Material) were normalized to values in young-adult WT mice and compared with old WT and J20 mice of both ages in the DG (B) and SUB (C). Significance differences were found in the DG between young WT and young J20, old WT and old J20, and young WT and old WT. In addition, significant differences were found in the SUB between old WT and old J20, and young WT and old WT. Comparison and significant differences are indicated in the figure and in the text. Abbreviations: AD, Alzheimer's disease; CB, calbindin; DG, dentate gyrus; SUB, subiculum; J20, AD mouse model; WT, wild type.

($F_{(1,29)} = 5.2$, $P = .03$) (Fig. 2B). In contrast, DG CB signals were significantly higher in old J20 mice ($F_{(1,40)} = -10.2$ $P = .003$). The subicular CB signal declined with age in WT mice ($F_{(1,34)} = 4.168$, $P = .012$), but its value was age independent in J20 mice ($F_{(1,35)} = 0.031$, $P = .972$) (Fig. 2C). CB IHC signal in J20 mice was significantly higher than that in WT in older mice ($F_{(1,40)} = -4.11$ $P = .013$) (Fig. 2C). In summary, our results indicate that CB levels do not decline in an age-dependent manner in the DG or subiculum of J20 mice, as it has been documented and corroborated here in WT mice, making the values of CB higher in the AD model than WT in older mice.

3.3. Age and amyloid pathology potentiate chronic Ca^{2+} dysregulation in apical dendrites

Resting Ca^{2+} level in neurons, as well as in other cells, is tightly controlled and is maintained by multiple mechanisms [32]. We compared resting Ca^{2+} values in WT, J20, and

CBKO mice and both ages and used a single wavelength Ca^{2+} indicator protocol as described in Supplementary Methods section. Data were analyzed with a LRM. Results revealed that compared with WT, the resting Ca^{2+} levels in BC apical dendrites were significantly higher in older J20 BC dendrites ($F_{(5,135)} = 3.319$, $P = .039$; WT versus J20, $P = .035$; CBKO versus J20, $P = .536$; WT versus CBKO, $P = .448$) (Fig. 3B). In addition, age did not affect resting Ca^{2+} levels in WT and CBKO neurons (WT, $P = .592$; CBKO, $P = .174$) (Fig. 3B). However, the increase in resting Ca^{2+} levels in old J20 BC dendrites indicated changes in Ca^{2+} handling (J20*age interaction, $P = .045$) (Fig. 3B).

3.4. Abnormalities in temporal dynamics of subicular calcium signals in dendrites of J20 and CBKO mice

We first studied the active and passive BC neurons' electrophysiological membrane properties of WT, J20, and CBKO mice and found no statistical differences between the genotypes (Supplementary Table 2) similar to previous studies in AD [33–35]. Next, experiments were performed in BC subicular neurons' apical dendrites to compare Ca^{2+} transient dynamics using OG1 (50 μM) in young and old mice (Fig. 3A). Fluorescence signals were collected from the apical dendrite. We compared peak calcium transients and monoexponential decay time constants. Analysis using LRM controlling for multiple comparisons showed that peak Ca^{2+} transients in apical dendrites (Fig. 1D) were similar in the three groups at young age ($F_{(2,112)} = 1.051$, $P = .353$), whereas the peak Ca^{2+} transient amplitudes were significantly smaller in old CBKO mice ($F_{(2,21)} = 4.285$, $P = .016$; WT versus CBKO, $P = .044$; J20 versus CBKO, $P = .026$) (Fig. 3C). A comparison of peak Ca^{2+} transients from the three groups demonstrated that aging did not affect this parameter in WT and J20 BC dendrites (WT, $P = .255$; J20, $P = .323$) (Fig. 3C). However, peak Ca^{2+} transient was significantly lower in old CBKO neurons (young vs. old, $P = .013$) (Fig. 3C).

LRM analysis shows that the monoexponential decay time constants were similar between the different groups at young age ($F_{(2, 58)} = 1.162$, $P = .317$) (Fig. 3D). Mono-exponential fittings of decay time constants of elder mice revealed those to be faster in CBKO and J20 dendrites than in WT neurons ($F_{(2, 21)} = 5.086$, $P = .008$; WT versus J20, $P = .024$; WT versus CBKO, $P = .005$) (Fig. 3D). The results demonstrate unexpected Ca^{2+} dynamics in J20 mice suggestive of compensatory processes, indicated by the age-related changes in decay time constants (faster). Similarly, old CBKO dendrites had findings suggestive of compensatory processes, as indicated by the lower peak Ca^{2+} transient and faster decay time constant in older mice, again an unexpected finding if the only calcium buffer modified was CB.

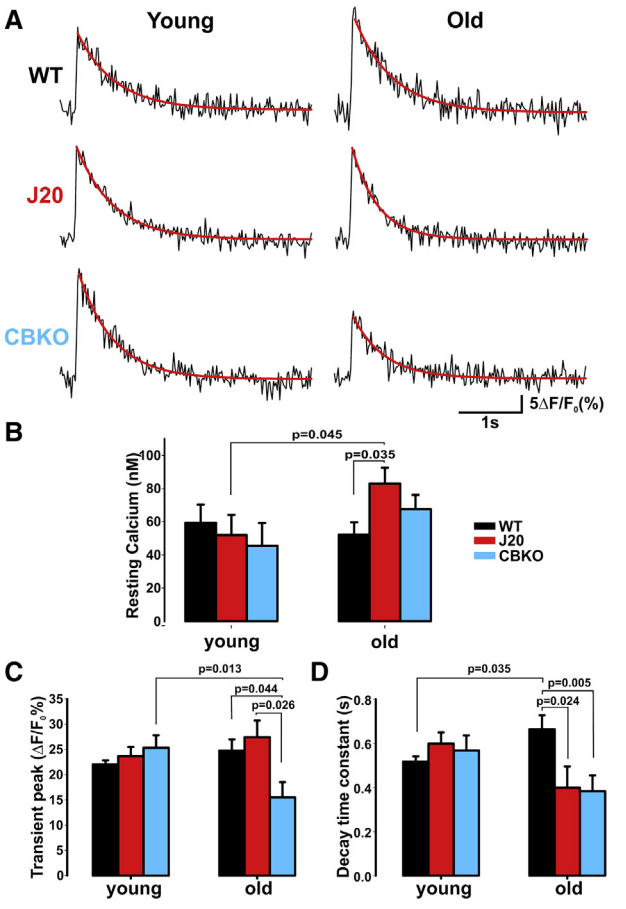

Fig. 3. Age- and genotype-related changes in Ca^{2+} dynamics and resting Ca^{2+} levels of BC subicular neurons in WT, J20, and CBKO mice. (A) Representative Ca^{2+} transients (OG1: 50 μM) in apical dendrites elicited by 3 rapid depolarization steps (100 Hz, 3 ms, from −70 mV to +10 mV) in subicular BC neurons of young-adult and older-adult WT (n = 86 and 12, respectively), J20 (n = 18 and 5, respectively), and CBKO (n = 10 and 6, respectively) mice. Shown are the traces in which the decay time constant (red line) is fitted with a single exponential function (approx. 50% of the cells in the three groups, see text). (B) Mean values + SEM of resting Ca^{2+} estimation (see methods) in different age groups and genotypes as indicated in the figure. Resting Ca^{2+} levels were similar at different groups in young-adult mice (WT n = 25, J20 n = 14, and n = 11). Old J20 mice subicular neuron dendrites show higher resting Ca^{2+} compared with all other groups (WT n = 36, J20 n = 23, and CBKO = 28). Age was a significant factor in J20 neurons, but not in WT or CBKO neurons. (C) Shown are mean and SEM values of peak Ca^{2+} transients at different ages in the different genotypes as indicated in the figure. Note that young mice have similar Ca^{2+} transient peaks, whereas old CBKO had significant smaller peaks than old WT and J20 groups. In addition, only CBKO had an age-dependent decrease of the peak Ca^{2+} transient in compare with WT and J20 groups. (D) Mono-exponential decay time constant (mean + SEM) from Ca^{2+} transients at different ages and in different genotypes. No significant differences between genotypes were observed in young mice. Old CBKO and J20 mice had a faster decay time constant as compared with old WT mice, and old WT mice have a slower decay than young WT mice. Abbreviations: AD, Alzheimer's disease; BC, bursting cells; CBKO, calbindin knock-out; DG, dentate gyrus; SUB, subiculum; J20, AD mouse model; WT, wild type.

3.5. Changes in the Ca^{2+}-buffering capacity of AD and CBKO subicular dendrites

The ability of subicular neurons to rapidly buffer depolarization-evoked Ca^{2+} influx (Ca^{2+}-buffering capacity) was studied comparatively in WT, J20, and CBKO mice. In these experiments, the endogenous buffer was titrated against incremental concentrations of OG1. The Ca^{2+}-buffering capacity is defined as the ratio of Ca^{2+} ions bound to a buffer over the free (unbound) Ca^{2+} ions (Supplementary Methods, Equation 3). Experiments were performed in old mice. First, we estimated the resting Ca^{2+} levels and decay time constants based on Ca^{2+} transients elicited by one and three APs at different concentrations of the Ca^{2+} probe (OG1 100, 50, 25, and 12.5 μM) (Fig. 4A). As expected, resulting from the buffer properties of OG1, changes in the decay time constants and peak Ca^{2+} transients were observed at different concentrations (Fig. 4B and C).

The Ca^{2+}-buffering capacity was estimated assuming a single compartment model [32]. Different concentrations of OG1 were used to estimate the exogenous Ca^{2+}-buffering capacity (plotted on the *x-axis*), and the decay time constant of Ca^{2+} transients elicited with three rapid depolarizations (3 APs) was plotted on the *y-axis*, and data were fitted with a linear regression. The *x*-intercept of the linear regression represents the internal Ca^{2+}-buffering capacity and was determined in the different groups (WT = 88, n = 37, r^2 = 0.83 $P < .001$; J20 = 168, n = 21, r^2 = 0.79 $P < .001$; CBKO = 58, n = 24, r^2 = 0.88 $P < .001$) (Fig. 4D, E, 4F). The decrease in the Ca^{2+}-buffering capacity of CBKO neurons was as expected by the removal of CB acting as Ca^{2+} buffer (WT = 88, CBKO = 58). The increased Ca^{2+}-buffering capacity found in subicular dendrites of J20 mice is consistent with the higher CB expression indirectly observed as a stronger CB IHC signal in the subiculum of old J20 mice (Fig. 2C), although other additional mechanisms may be implicated.

3.6. Low-affinity Ca^{2+} indicator–based experiments identify additional abnormalities in Ca^{2+} dynamics in J20 and CBKO mice

The low-affinity Ca^{2+} indicator OG-5N (K_D = 20 μM) was used for the following set of experiments, to extend

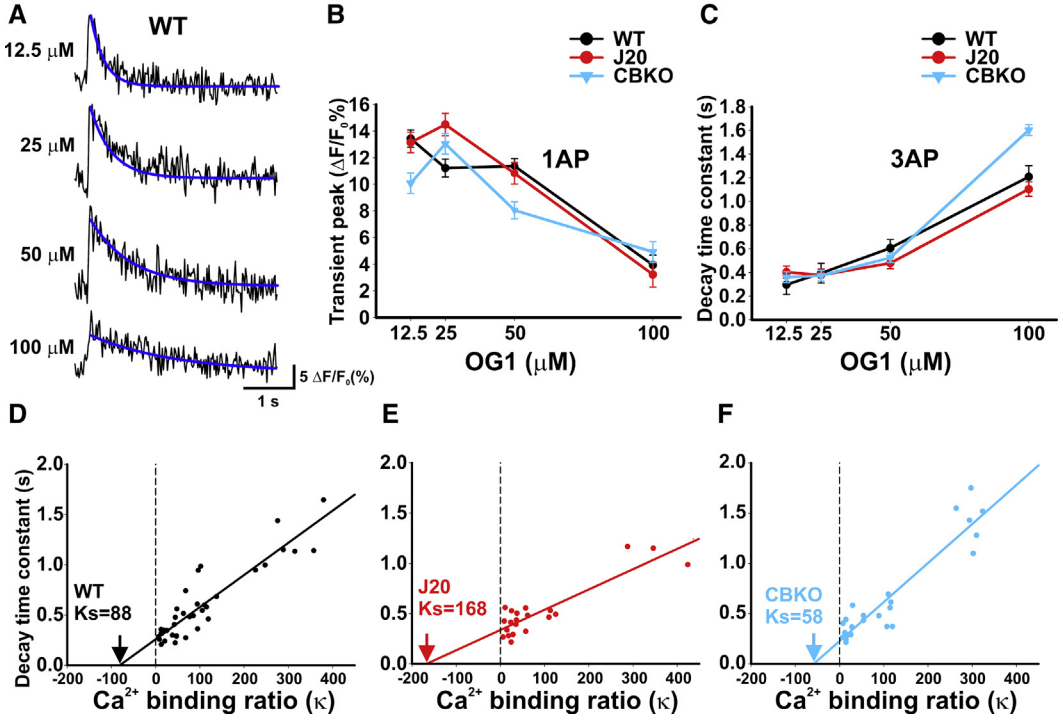

Fig. 4. Estimation of the Ca^{2+}-buffering capacity in apical dendrites of subicular BC neurons from different genotypes in old mice. (A) Representative Ca^{2+} transients evoked with a single depolarization using different concentrations of OG1 in the pipette (12.5, 25, 50, and 100 μM, as indicated). Mono-exponential fitting is in dark blue. Note that, as expected, the decay time constant is slower with higher OG1 concentrations in all neurons recorded. (B) Mean + SEM of peak Ca^{2+} concentrations at different concentrations of OG1 in the three genotypes (indicated in the graph), elicited with a single depolarization (1AP) (3 ms, from −70 mV to +10 mV). (C) Mean + SEM of Ca^{2+} transients decay time constants elicited with 3 rapid depolarizations (3AP) (100 Hz, 3 ms, from −70 mV to +10 mV). Data obtained from these transients were used to estimate the Ca^{2+}-buffering capacity in the different genotypes. (D-F) Individual neuron kappa values (see Methods and Supplementary Methods) were plotted against the decay time constant of a Ca^{2+} transient after three rapid depolarizations (3AP). Linear regression was performed, and the interception with the *x-axis* was considered as the estimated endogenous buffering capacity in the apical dendrite for the 3 groups of neurons, as indicated. (D) WT κ_S: 88, n = 37 cells, r^2: 0.83; $P < .001$. (E) J20 κ_S: 168, n = 21 cells, r^2: 0.79; $P < .001$. (F) CBKO κ_S: 58, n = 24 cells, r^2: 0.88; $P < .001$. Abbreviations: AD, Alzheimer's disease; BC, bursting cells; CBKO, calbindin knock-out; DG, dentate gyrus; SUB, subiculum; J20, AD mouse model; WT, wild type; OG1, Oregon Green 488 BAPTA-1.

the findings presented previously with a different probe in BC dendrites of old mice. The advantages of Oregon Green 488 BAPTA-5N for these experiments are (1) less interference with the internal Ca^{2+} buffers and (2) lower saturation probability. A disadvantage is the relatively smaller evoked transients given its kinetics, which decreases the signal-to-noise ratio. For this reason, we induced a large Ca^{2+} transient by a train of depolarizing steps (125 Hz for 7 seconds, and comparisons were performed for the last 500 ms of the stimulation period (Fig. 5A and B). WT subicular BC dendrites reached a significantly lower Ca^{2+} plateau level compared with J20 and CBKO neurons (WT = 46.61 ± 0.86 %$\Delta F/F_0$; J20 = 70.71 ± 1.71 %$\Delta F/F_0$; CBKO = 67.60 ± 1.39 %$\Delta F/F_0$; analysis of variance $F_{(2,14)} = 13{,}79$, $P < .01$; Post hoc Games-Howell WT versus J20 $P < .01$; WT versus CBKO $P < .01$) (Fig. 5A and B). In contrast, the Ca^{2+} plateau level was similar between the J20 and CBKO subicular dendrites (J20 vs. CBKO $P = .339$). These findings indicate a deficiency in both CBKO and J20 to cope with, i.e., to buffer high Ca^{2+} levels.

3.7. Modeling of intracellular Ca^{2+} dynamics in young and old WT, CBKO and AD mice

We performed reaction-diffusion and electrical modeling of a multicompartmental pyramidal neuron. To simulate Ca^{2+} transients, we modeled OG-1, using kinetic parameters taken from the literature (see Supplementary Methods). In the model, we used the same concentration of OG-1 as was used in the experiments, as well as the same temperature (24°C).

To generate Ca^{2+} transients, we placed a voltage clamp in the soma (100-130 ms) set to 80 mV above the resting membrane potential. The depolarized membrane potential caused opening of voltage-gated Ca^{2+} channels, influx of extracellular Ca^{2+}, and binding of this Ca^{2+} to simulated OG, forming a Ca^{2+}/OG (CaOG) complex, whose concentration reflects the free intracellular Ca^{2+} concentration. We quantified properties of the CaOG transient and compared them with experimental results. Both the concentrations of the different Ca^{2+} buffers (CB and other nonspecific buffers) and the rate of Ca^{2+} extrusion by pumps influenced the CaOG transient decay time constant (τ), the peak [CaOG] during a Ca^{2+} transient, and the resting (basal) Ca^{2+} levels.

We adjusted parameters in the simulations to replicate the direction of changes of each of the four investigated features of a Ca^{2+} transient (temporal changes in [CaOG], τ, peak [CaOG], and resting intracellular [Ca^{2+}]) observed in experiments as a function of age. The underlying changes required to replicate the experimental data suggest the induction of several different homeostatic mechanisms that regulate Ca^{2+} levels. In WT, we simulated young mice to have equal levels of CB and other nonspecific Ca^{2+} buffers. To simulate normal aging in WT, we reduced levels of CB and other Ca^{2+} buffers. As a possibly homeostatic compensation, we needed to increase the Ca^{2+} extrusion pump rate. This then resulted in a faster half-decay time τ, a slightly higher peak [CaOG] and a lower basal Ca^{2+} level in the older mice, as was observed experimentally (Fig. 6, top row, A-D).

In the next set of simulations, we modeled CBKO mice by setting the intracellular CB concentration to 0 mM. We hypothesized that CBKO mice might have higher levels of other Ca^{2+} buffers as a compensatory possibly "protective" mechanism. This increase in "other Ca^{2+} buffers" was sufficient to rather accurately model the Ca^{2+} transients in young CBKO resulting in transients as observed in young WT. To model the situation prevailing in old CBKO, we increased the nonspecific Ca^{2+} buffer concentrations, reduced voltage-gated Ca^{2+} channel density, and increased the extrusion rates of Ca^{2+} pumps. As a result of these changes, Ca^{2+} transients decayed much more rapidly, with lower peak values, when we reduced the efficacy of the Ca^{2+} extrusion pump marginally (see Supplementary Methods). This caused a slight increase in basal Ca^{2+} levels (Fig. 6, middle row A-D). All the changes in old CBKO mice were also consistent with experiments.

Finally, we modeled the Ca^{2+} transients in young and old J20 mice. We hypothesized that Ca^{2+}-mediated excitotoxicity might cause neuronal damage leading to AD, but that J20 mice would demonstrate homeostatic compensatory mechanisms, including maintenance of CB levels also at old age. Thus, CB and nonspecific Ca^{2+} buffer levels in the young

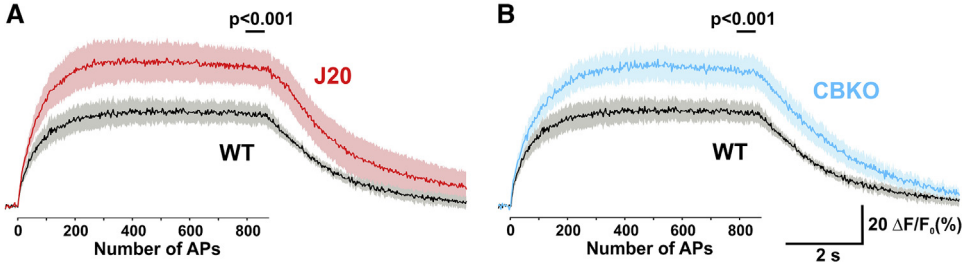

Fig. 5. J20 and CBKO mice have deficiencies to buffer a large Ca^{2+} influx. Oregon Green BAPTA-5N (OG5N; 500 μM) was used as a low-affinity Ca^{2+} dye, to measure the dynamics of high Ca^{2+} concentrations. (A) Ca^{2+} transients evoked with a prolonged depolarization (100 Hz, 3 ms for 7 s) in J20 (red traces; n = 5) and WT (black traces; n = 5) subicular BC neurons. (B) Same as in A, but comparing CBKO (blue traces; n = 6) and WT. Notice that both CBKO and J20 mice have higher plateau values after the initial 5 APs, indicating that Ca^{2+} buffering is decreased for large Ca^{2+} influx. Abbreviations: AP, action potential; CBKO, calbindin knock-out; J20, Alzheimer's disease mouse model; WT, wild type.

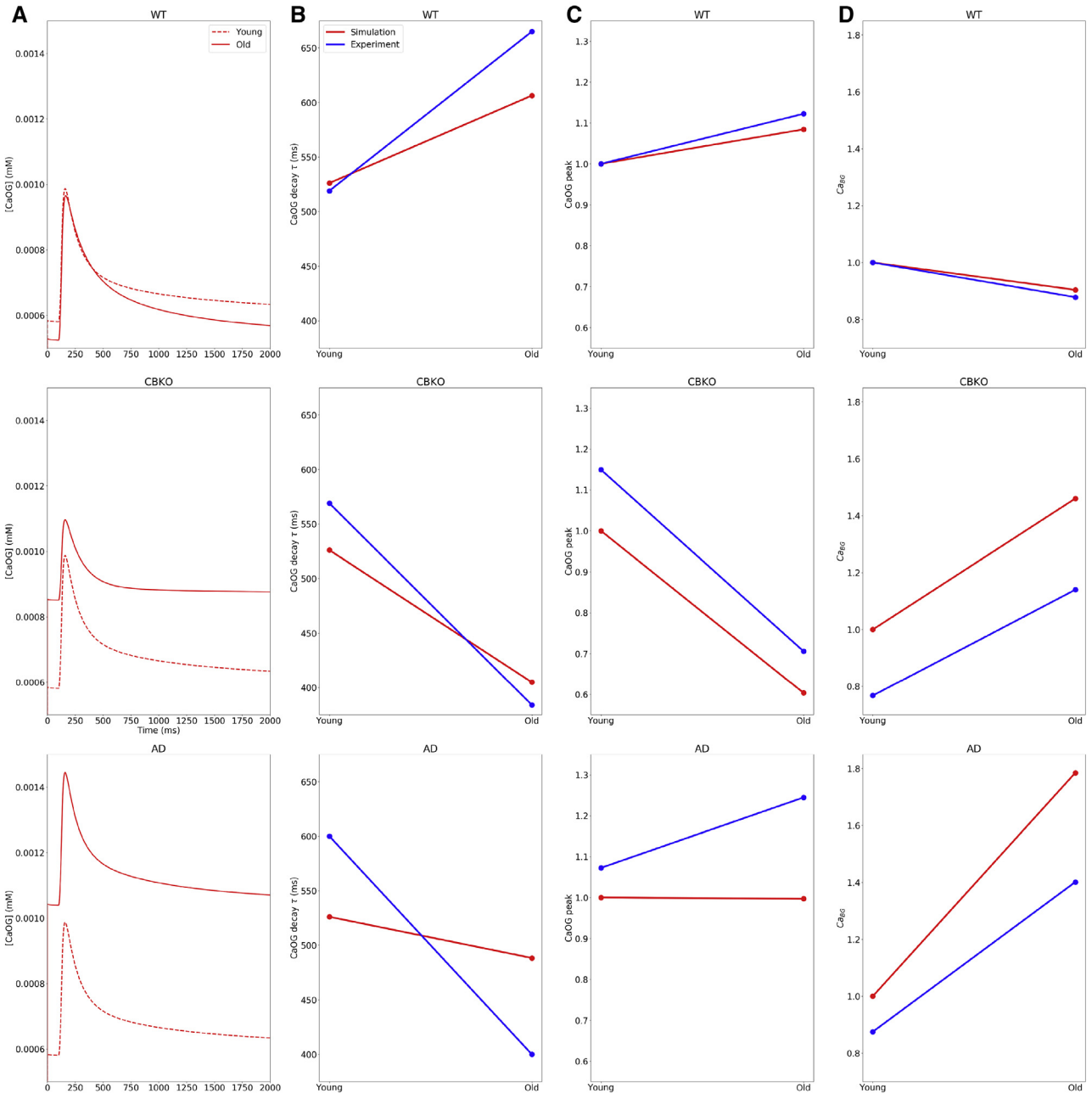

Fig. 6. Computer simulations predict several different homeostatic mechanisms that compensate for Ca^{2+} dysregulation in CBKO and J20 mice. Somatic voltage clamp (100–130 ms; 80 mV above resting membrane potential) causes opening of voltage-gated Ca^{2+} channels, influx of Ca^{2+}, and binding of Ca^{2+} to Oregon Green (OG), forming CaOG complexes. Concentrations of the latter are reflecting the changes in cytosolic Ca^{2+} concentrations in WT (first row), CBKO (second row), and the AD model (J20 mice) of young (stippled line) and old (solid line) mice (A). Both the concentrations of the different Ca^{2+} buffers and the rate of Ca^{2+} extrusion pumps influence (B) the CaOG transient decay time constant, (C) the peak CaOG transient, and (D) the resting (basal) Ca^{2+} levels. Simulations (red) replicated the direction of changes of the variables observed in experiments (blue; B-D) as a function of the age of mice. Model-predicted mechanisms are described. Top row: wild-type (WT): young—equal levels of CB and other Ca^{2+} buffers; old—reduced levels of CB and other Ca^{2+} buffers, minor increase in speed of Ca^{2+} extrusion to compensate for reduced Ca^{2+} buffering. Middle row: CB knockout mice (CBKO): young—loss of CB produces higher levels of other Ca^{2+} buffers to compensate for loss of CB; old—intermediate reduction in efficacy of Ca^{2+} extrusion pump moderately raises resting Ca^{2+} levels, further results in increases in other Ca^{2+} buffers, a reduced voltage-gated Ca^{2+} channel (VGCC) density, and an increase in speed of Ca^{2+} extrusion, possibly to protect against effects of aging and loss of CB. Bottom row: Alzheimer's disease (AD): young—minimal changes in Ca^{2+} buffers; old—reduced efficacy of Ca^{2+} extrusion pump substantially raises resting Ca^{2+} levels, homeostatic maintenance of CB levels and major increase in speed of Ca^{2+} extrusion, in parallel with reduction in other Ca^{2+} buffer levels due to aging.

AD mice were kept identical to the ones of young WT mice. In the old J20 mice, we simulated homeostatic mechanisms by maintaining CB levels and by a major increase in the speed of Ca^{2+} extrusion, while decreasing the nonspecific Ca^{2+} buffer levels. In addition, in the old J20 mice, we reduced the Ca^{2+} extrusion pump efficacy substantially (see Supplementary Methods).

As a result of these modeled changes, the old J20 mice showed faster CaOG transients. The experimentally observed higher peak [CaOG] was not accurately modeled; however, due to reduced Ca^{2+} extrusion pump efficacy, there was a large increase in basal Ca^{2+} levels, in agreement with experimental data (Fig. 6, lower row, A-D).

4. Discussion

This is the first report of subicular neuron Ca^{2+} dynamics in WT or an AD mouse model. Similar to reports on rats [7,36], we found that the majority of subicular neurons were BC. BC and RS were found to show differences in electrophysiological properties, but not in intracellular Ca^{2+} handling. The lower input resistance is likely to decrease BC neuron excitability compared with RS. A higher input resistance in RS neurons but similar resting potentials in both cell types was previously demonstrated in young [36] and in older rats [7]. Importantly, similarities of resting Ca^{2+} and Ca^{2+} transient decay time constants between BC and RS neurons indicate that the Ca^{2+} signaling machinery has closely related kinetics. Although it is established that the subiculum is affected early in AD [3,37], the specific neuronal subpopulation remains unknown.

The presented Ca^{2+} measurements report the volume-averaged Ca^{2+} (Ca_i), which is the Ca^{2+} concentration assumed to be homogenous within a small-size cellular compartment one millisecond after the Ca^{2+} influx/release [38]. Such Ca_i measurements are affected by Ca^{2+}-buffer proteins such as CB [30] and by the Ca^{2+} indicator [32]. No significant changes were found in Ca^{2+} transients with single exponential decay time constant of young J20 mice compared with WT. As most of the subicular neurons are BC with similar peak Ca^{2+} transients, we presume no significant changes in the expression of CB in the two BC neuron subpopulations.

Surprisingly, the absence of CB in old CBKO neurons led to decreased peak Ca^{2+} transients. This strongly indicates alterations of the Ca^{2+} signaling toolkit, possibly as a compensatory mechanism. Such mechanisms have been reported in double knockout mice for CB and parvalbumin [39]. Consistent with reports in humans, our CB expression levels also decreased in the subiculum of WT mice during normal aging, which is correlated with regional vulnerability [40]. Interestingly, the significant age-dependent decrease in CB expression of WT subicular neurons was not reflected in transient peak Ca^{2+} changes (Fig. 3C), indicative of additional variations in the Ca^{2+} homeostasis in aged WT neurons.

Based on our data, we suggest that faster mono-exponential decay time constant values might be linked with higher CB expression levels in subicular neurons from old J20 mice compared with old WT neurons (Fig. 3D). This might be viewed as a compensatory mechanism, but certainly not the cause of the increased resting Ca^{2+} levels in old J20 neurons (Fig. 3B).

In our experiments, resting Ca^{2+} levels were increased in an age-related manner in J20 subicular neurons and were higher than in old WT neurons, which is previously reported in amyloidogenic models of AD [41,42]. It is known that Ca^{2+}-pump/exchangers and Ca^{2+} stores can affect resting Ca^{2+} levels [43,44], and we explored them with computer modeling (see Fig. 6). Resting Ca^{2+} levels in CBKO subicular neurons were unaffected; CB is a moderate-to-fast high-affinity Ca^{2+} buffer and is not expected to affect resting Ca^{2+} levels [30].

To the best of our knowledge, there are no previous reports of the Ca^{2+}-buffering capacity of neurons in AD. In general, the Ca^{2+}-buffering capacity in WT subicular dendrites is within the range found in previous reports from dendrites of hippocampal pyramidal neurons [21,45]. We found that the Ca^{2+}-buffering capacity was significantly higher in old J20 neurons than in WT neurons (Fig. 4D, E). Also, it has been previously reported that Ca^{2+}-buffering capacity during normal aging is increased in several neuron types [45,46,47]. An increased Ca^{2+}-buffering capacity is thought to be a protective mechanism during normal "physiological" aging [18]. In line with these previous reports and with the high Ca^{2+}-buffering capacity of J20 neurons, J20 mice shows minimal neuronal death in the CA3 subregions even at old age [48].

Our experiments and modeling predict several homeostatic mechanisms that might counteract the different forms of Ca^{2+} imbalance including reductions in voltage-gated Ca^{2+} channel density, increases in Ca^{2+}-buffer concentrations, and changes in the rate of Ca^{2+} extrusion pumps. In addition, the model predicts that Ca^{2+} extrusion pump efficacy is reduced with aging in both CBKO and AD mice, producing noticeable increases in resting Ca^{2+} levels observed mainly in the AD model. Such mechanisms have been suggested previously [43,44]; however, our modeling ties each homeostatic change with a specific experimental condition.

Finally, the early decline in the CB expression level is not a critical factor for the subiculum dysfunction/susceptibility in J20 mice. Further study is required to assess whether maintenance of high levels of CB in subicular neurons is a physiological homeostatic response in AD.

Acknowledgments

The authors would like to acknowledge Dr. I. Llano from Université Paris 5, Paris, for her help throughout the project. NIH, NIA Grant AG051556 to HM. NIH, NIDCD Grant 2R01DC012947-06A1 to S.A.N.

Supplementary Data

Supplementary data related to this article can be found at https://doi.org/10.1016/j.jalz.2019.07.017.

RESEARCH IN CONTEXT

1. Systematic review: Although the link between specific brain region susceptibility and the pathophysiology of Alzheimer' disease (AD) is not well understood, the neuronal calcium changes in AD have been well documented. Here, we reviewed recent publications describing the region-specific changes in Ca^{2+} binding proteins and Ca^{2+} dyshomeostasis in AD, and those focused in the subiculum and adjacent regions.
2. Interpretation: This study modifies the general view in the AD community, which proposes that decreased expression of Ca^{2+} buffer is critical in AD-related Ca^{2+} dyshomeostasis. Specifically, we showed an unexpected age-related increased Ca^{2+} buffering capacity in subicular neurons of AD mice, and the opposite in calbindin knock-out mice.
3. Future directions: We propose that Ca^{2+} overload leads to increased Ca^{2+}-buffering capacity because of compensatory mechanisms. Our modeling indicates that abnormalities in Ca^{2+} extrusion systems could explain it. Therefore, future experiments must elucidate the upregulated Ca^{2+} buffer/extrusion system and its subcellular localization; the mechanism of such process; and the processes regulating this compensatory event, which may provide insights into new therapeutic approaches.

References

[1] Tarawneh R, Holtzman DM. The clinical problem of symptomatic Alzheimer disease and mild cognitive impairment. Cold Spring Harb Perspect Med 2012;2:a006148.
[2] Davies DC, Wilmott AC, Mann DM. Senile plaques are concentrated in the subicular region of the hippocampal formation in Alzheimer's disease. Neurosci Lett 1988;94:228–33.
[3] Schonheit B, Zarski R, Ohm TG. Spatial and temporal relationships between plaques and tangles in Alzheimer-pathology. Neurobiol Aging 2004;25:697–711.
[4] Rossler M, Zarski R, Bohl J, Ohm TG. Stage-dependent and sector-specific neuronal loss in hippocampus during Alzheimer's disease. Acta Neuropathol 2002;103:363–9.
[5] Trujillo-Estrada L, et al. Early neuronal loss and axonal/presynaptic damage is associated with accelerated amyloid-beta accumulation in AβPP/PS1 Alzheimer's disease mice subiculum. J Alzheimers Dis 2014;42:521–41.
[6] Angulo SL, Orman R, Neymotin SA, Liu L, Buitrago L, Cepeda-Prado E, et al. Tau and amyloid-related pathologies in the entorhinal cortex have divergent effects in the hippocampal circuit. Neurobiol Dis 2017;108:261–76.
[7] Kim Y, Spruston N. Target-specific output patterns are predicted by the distribution of regular-spiking and bursting pyramidal neurons in the subiculum. Hippocampus 2012;22:693–706.
[8] Khachaturian ZS. Hypothesis on the regulation of cytosol calcium concentration and the aging brain. Neurobiol Aging 1987;8:345–6.
[9] Busche MA, Chen X, Henning HA, Reichwald J, Staufenbiel M, Sakmann B, et al. Critical role of soluble amyloid-beta for early hippocampal hyperactivity in a mouse model of Alzheimer's disease. Proc Natl Acad Sci U S A 2012;109:8740–5.
[10] Lopez JR, et al. Increased intraneuronal resting [Ca2+] in adult Alzheimer's disease mice. J Neurochem 2008;105:262–71.
[11] Shilling D, et al. Suppression of InsP3 receptor-mediated Ca2+ signaling alleviates mutant presenilin-linked familial Alzheimer's disease pathogenesis. J Neurosci 2014;34:6910–23.
[12] Oules B, Del Prete D, Greco B, Zhang X, Lauritzen I, Sevalle J, et al. Ryanodine receptor blockade reduces amyloid-beta load and memory impairments in Tg2576 mouse model of Alzheimer disease. J Neurosci 2012;32:11820–34.
[13] Wang Y, Mattson MP. L-type Ca2+ currents at CA1 synapses, but not CA3 or dentate granule neuron synapses, are increased in 3xTgAD mice in an age-dependent manner. Neurobiol Aging 2014;35:88–95.
[14] Sun S, Zhang H, Liu J, Popugaeva E, Xu NJ, Feske S, et al. Reduced synaptic STIM2 expression and impaired store-operated calcium entry cause destabilization of mature spines in mutant presenilin mice. Neuron 2014;82:79–93.
[15] Palop JJ, et al. Neuronal depletion of calcium-dependent proteins in the dentate gyrus is tightly linked to Alzheimer's disease-related cognitive deficits. Proc Natl Acad Sci U S A 2003;100:9572–7.
[16] Odero GL, et al. Evidence for the involvement of calbindin D28k in the presenilin 1 model of Alzheimer's disease. Neuroscience 2010; 169:532–43.
[17] Riascos D, et al. Age-related loss of calcium buffering and selective neuronal vulnerability in Alzheimer's disease. Acta Neuropathol 2011;122:565–76.
[18] Kook SY, Jeong H, Kang MJ, Park R, Shin HJ, Han SH, et al. Crucial role of calbindin-D in the pathogenesis of Alzheimer's disease mouse model. Cell Death Differ 2014;21:1575–87.
[19] Celio MR. Calbindin D-28k and parvalbumin in the rat nervous system. Neuroscience 1990;35:375–475.
[20] Fierro L, Llano I. High endogenous calcium buffering in Purkinje cells from rat cerebellar slices. J Physiol 1996;496:617–25.
[21] Maravall M, Mainen ZF, Sabatini BL, Svoboda K. Estimating intracellular calcium concentrations and buffering without wavelength ratioing. Biophys J 2000;78:2655–67.
[22] Neymotin SA, et al. Calcium regulation of HCN channels supports persistent activity in a multiscale model of neocortex. Neuroscience 2016;316:344–66.
[23] Neymotin SA, McDougal RA, Bulanova AS, Zeki M, Lakatos P, Terman D, et al. Neuronal calcium wave propagation varies with changes in endoplasmic reticulum parameters: a computer model. Neural Comput 2015;27:898–924.
[24] Carnevale NT, Hines ML. The NEURON Book 2006. Cambridge University Press; 2006.
[25] McDougal RA, Hines ML, Lytton WW. Reaction-diffusion in the NEURON simulator. Front Neuroinform 2013;7:28.
[26] Hines ML, Morse T, Migliore M, Carnevale NT, Shepherd GM. ModelDB: a database to support computational neuroscience. J Comput Neurosci 2004;17:7–11.
[27] Staff NP, et al. Resting and active properties of pyramidal neurons in subiculum and CA1 of rat hippocampus. J Neurophysiol 2000; 84:2398–408.
[28] Collin T, et al. Developmental changes in parvalbumin regulate presynaptic Ca2+ signaling. J Neurosci 2005;25:96–107.

[29] Mucke L, Masliah E, Yu GQ, Mallory M, Rockenstein EM, Tatsuno G, et al. High-level neuronal expression of Aβ 1-42 in wild-type human amyloid protein precursor transgenic mice: synaptotoxicity without plaque formation. J Neurosci 2000;20:4050–8.
[30] Schwaller B. Cytosolic Ca2+ buffers. Cold Spring Harb Perspect Biol 2010;2:a004051.
[31] Moreno H, Burghardt NS, Vela-Duarte D, Masciotti J, Hua F, Fenton AA, et al. The absence of the calcium-buffering protein calbindin is associated with faster age-related decline in hippocampal metabolism. Hippocampus 2012;22:1107–20.
[32] Neher E, Augustine GJ. Calcium gradients and buffers in bovine chromaffin cells. J Physiol 1992;450:273–301.
[33] Rocher AB, Kinson MS, Luebke JI. Significant structural but not physiological changes in cortical neurons of 12-month-old Tg2576 mice. Neurobiol Dis 2008;32:309–18.
[34] Stern EA, Bacskai BJ, Hickey GA, Attenello FJ, Lombardo JA, Hyman BT. Cortical synaptic integration in vivo is disrupted by amyloid-beta plaques. J Neurosci 2004;24:4535–40.
[35] Tamagnini F, et al. Intrinsic excitability changes induced by acute treatment of hippocampal CA1 pyramidal neurons with exogenous amyloid beta peptide. Hippocampus 2015;25:786–97.
[36] van Welie I, et al. Different levels of Ih determine distinct temporal integration in bursting and regular-spiking neurons in rat subiculum. J Physiol 2006;576:203–14.
[37] Oakley H, Cole SL, Logan S, Maus E, Shao P, Craft J, et al. Intraneuronal beta-amyloid aggregates, neurodegeneration, and neuron loss in transgenic mice with five familial Alzheimer's disease mutations: potential factors in amyloid plaque formation. J Neurosci 2006;26:10129–40.
[38] Meinrenken CJ, Borst JG, Sakmann B. Local routes revisited: the space and time dependence of the Ca2+ signal for phasic transmitter release at the rat calyx of Held. J Physiol 2003;547:665–89.
[39] Kreiner L, Christel CJ, Benveniste M, Schwaller B, Lee A. Compensatory regulation of Cav2.1 Ca2+ channels in cerebellar Purkinje neurons lacking parvalbumin and calbindin D-28k. J Neurophysiol 2010;103:371–81.
[40] Geula C, et al. Loss of calbindin-D28k from aging human cholinergic basal forebrain: relation to neuronal loss. J Comp Neurol 2003;455:249–59.
[41] Busche MA, et al. Clusters of hyperactive neurons near amyloid plaques in a mouse model of Alzheimer's disease. Science 2008;321:1686–9.
[42] Kuchibhotla KV, et al. Synchronous hyperactivity and intercellular calcium waves in astrocytes in Alzheimer mice. Science 2009;323:1211–5.
[43] Berrocal M, et al. Calmodulin antagonizes amyloid-beta peptides-mediated inhibition of brain plasma membrane Ca(2+)-ATPase. Biochim Biophys Acta 2012;1822:961–9.
[44] Kim MH, et al. Interplay between Na+/Ca2+ exchangers and mitochondria in Ca2+ clearance at the calyx of Held. J Neurosci 2005;25:6057–65.
[45] Oh MM, Oliveira FA, Waters J, Disterhoft JF. Altered calcium metabolism in aging CA1 hippocampal pyramidal neurons. J Neurosci 2013;33:7905–11.
[46] Stocca G, Schmidt-Hieber C, Bischofberger J. Differential dendritic Ca2+ signalling in young and mature hippocampal granule cells. J Physiol 2008;586:3795–811.
[47] Murchison D, Griffith WH. Increased calcium buffering in basal forebrain neurons during aging. J Neurophysiol 1998;80:350–64.
[48] Wright AL, Zinn R, Hohensinn B, Konen LM, Beynon SB, Tan RP, et al. Neuroinflammation and neuronal loss precede Aβ plaque deposition in the hAPP-J20 mouse model of Alzheimer's disease. PLoS One 2013;8:e59586.